Forces and torques on a prolate spheroid: low-Reynolds number and attack angle effects

Helge I. Andersson[1], Fengjian Jiang[2*]

[1]Department of Energy and Process Engineering, Norwegian University of Science and Technology (NTNU), 7491 Trondheim, Norway
[2]Department of Marine Technology, NTNU, 7491 Trondheim, Norway
* Corresponding author: fengjian.jiang@ntnu.no

Abstract
The three-dimensional flow field around a prolate spheroid has been obtained by integration of the full Navier-Stokes equations at Reynolds numbers 0.1, 1.0 and 10. The 6:1 spheroid was embedded in a Cartesian mesh by means of an immersed boundary method. In the low-Re range, due to the dominance of viscous stresses, an exceptionally wide computational domain was required, together with a substantial grid refinement in vicinity of the surface of the immersed spheroid. Flow fields in equatorial and meridional planes were visualized by means of streamlines to illustrate Reynolds number and attack angle effects. Drag and lift forces and torques were computed and compared with the most recent correlation formulas. The largest discrepancies were observed for the moment coefficient whereas the drag coefficient compared reasonably well.

Key words: Inclined spheroids; Reynolds number effects; Computational challenges; Force and torque coefficients

1 Introduction

1.1 Background

Solid particles embedded in a viscous fluid are encountered in a variety of different settings, both in industrial processes and in nature. Two notable examples of environmental concern are droplets in clouds (Shaw [40]) and microplastics in the ocean (Barboza and Gimenez [7]). Depending on the actual situation, the particles may either passively follow the flow as tracer particles, or lead or lag behind the fluid motion. Inertial particles are known to exhibit a slip velocity relative to the local fluid provided that the particle relaxation time is relatively large compared to a representative time scale of the fluid motion. The ratio between these two time scales is commonly referred to as the Stokes number. Besides particle inertia, parameterized by the Stokes number, the shape of the solid particle is another factor of major importance. Although the vast majority of investigations assumed the particles to be spheres, non-spherical particles are frequently encountered; see e.g. Andersson and Soldati [1] and Voth and Soldati [47]. A non-spherical particle is often modelled as either a finite-length circular cylinder or an ellipsoid. Most commonly axisymmetric ellipsoids, i.e. spheroids, are considered. In practice, however, also irregularly shaped particles are occurring in many industrial processes, as discussed by Sommerfeld and Qadir [43].

1.2 Computational modelling approaches

A variety of different approaches are used to simulate particle-laden flows; see e.g. the best-practice guidelines by Sommerfeld et al. [42]. Here, we are only concerned with hybrid Lagrangian-Eulerian methods, in which the flow field is obtained by solving the Navier-Stokes equations in an inertial frame of reference, whereas the suspended particles are treated individually and tracked in a Lagrangian framework. The choice of mathematical modelling of the solid particles depends on their characteristic size δ as compared with the size of the smallest flow structures η, which in a turbulent environment is known as the so-called Kolmogorov length scale. Distinctions have to be made between sub-Kolmogorov-scale particles ($\delta/\eta \ll 1$), Kolmogorov-sized particles ($\delta \approx \eta$), and Taylor-scale-sized particles ($\delta/\eta \gg 1$).

1.2.1 Point-particles

Particulate additives to a continuous fluid can be treated as point-particles provided that their size δ is smaller than the tiniest turbulent eddies, i.e. $\delta \ll \eta$. This assumption is justified in several different applications, for instance for planktonic organisms in the ocean. According to Durham et al. [12] the size of typical phytoplankton cells are $\delta \sim 1 - 100 \, \mu m$, whereas the Kolmogorov length scale $\eta \sim 0.1 - 10 \, mm$ in marine turbulence; see e.g. Jiménez [25]. In addition to the size constraint, $\delta/\eta \ll 1$, common practice requires that the particle Reynolds number Re_p has to be smaller than one. The latter requirement is essential in order to utilize analytically derived expressions for the viscous forces and torques acting on a solid particle submerged in a Stokes flow. In the limit as Re_p tends to zero, the flow in the immediate vicinity of a particle can be considered as Stokesian, the non-linear terms in the governing equations of motion are negligible, and the resulting set of linear equations becomes amenable to analytical treatment. Exact formulas for the viscous force and torque on an ellipsoidal particle were derived by Brenner [9] and Jeffery [22], respectively. A comprehensive treatise on the general subject of low-Re flows was provided by Happel and Brenner [19].

These force and torque expressions were adopted by Zhang et al. [51], Mortensen et al. [30], and Marchioli et al. [28] to simulate the behaviour of several thousands of prolate spheroids suspended in turbulent channel flow. The individually modelled spheroids translate and rotate in accordance with the viscous forces and torques exerted on them. Although the point-particle approach was first developed for tiny spherical particles, see *e.g.* Eaton [13], the recent review by Voth and Soldati [47] illustrates how the approach has been further developed and adopted also for non-spherical particles. Advantages and shortcomings of the point-particle approach to simulate dispersed multiphase flows were discussed in review articles by Balachandar [5], Eaton [13], and Balachandar and Eaton [6].

An obvious limitation of the point-particle approach is that the analytically derived expressions for the force and torque components are formally valid only for $Re_p = 0$. However, the Stokes drag force on a spherical particle remains a good

approximation at $Re_p = 0.1$ and nearly up to $Re_p = 1$. The same reasoning is often carried over to non-spherical particles, although yet without any rigorous proof of evidence.

1.2.2 Finite-sized particles

For larger particles, i.e. when the particle size δ is larger than the Kolmogorov length scale η, the point-particle approach can no longer be justified. For particles of size comparable with the Taylor-length scale λ, i.e. $\delta \approx \lambda >> \eta$, each particle can be treated as a solid body moving in the viscous fluid. Such finite-sized particles occupy parts of the computational volume and the surface of each particle has to be embedded in the computational mesh on which the flow field is computed. Four different approaches to resolve numerically the flow around individually moving particles were summarized by Lucci et al. [26] whereas a more comprehensive review was provided by Maxey [29]. One decade ago, these methods were only used to simulate finite-size spheres in turbulence. More recently, however, Do-Quang et al. [11] and Eshghinejadfard et al. [15] used a lattice-Boltzmann (LB) method to simulate the translational and rotational motion of elongated particles in turbulent channel flow. Do-Quang et al. [11] considered cylindrical particles with aspect ratios from 2 to 15, whereas Eshghinejadfard et al. [15] studied prolate spheroids with aspect ratio 1, 2 and 4. Ardekani et al. [4], by means of an immersed boundary (IB) method, showed that finite-sized oblate spheroids with aspect ratio 1:3 could lead to drag reduction. Eshghinejadfard et al. [16] attributed the drag reduction achieved by 1:3 oblate spheroids to the reduction of transverse fluid velocity fluctuations and enhancement of the spanwise streak spacing. These different approaches to resolved finite-size particle simulations require additional computational efforts for proper treatment of the solid surface of each of the moving particles. The number of particles in such simulations are therefore limited by the available hardware and typically of the order of 10 000.

1.2.3 Kolmogorov-sized particles

The point-particle approach cannot be justified for particles $\delta \geq \eta$ whereas the resolved particle approach becomes computationally too demanding for $\delta \leq \eta$. Unfortunately, many particles encountered in various applications are of a size δ comparable with the Kolmogorov length scale η, i.e. $\delta \approx \eta$. Very recently, Schneiders et al. [38], [39] advocated a novel approach to facilitate direct particle-fluid simulations (DPFS) of Kolmogorov-sized particles, in which the flow field over each particle is fully resolved by direct numerical simulations of the conservation equations. The particle surfaces are discretely resolved by means of a Cartesian cut-cell method. Particle-resolved simulations of 45 000 spherical particles were reported by Schneiders et al. [38] and of 45 000 prolate spheroids with aspect ratio 2 by Schneiders et al. [39]. An interesting assessment of the point-particle approach to non-spherical particles by means of DPFS-results in decaying turbulence was presented by Frölich et al.[17].

1.3 Extending the point-particle approach

A viable extension of the point-particle approach to particle Reynolds numbers Re_p of the order of unity and even above 1 is to generalize the analytically derived formulas for the force and torque components of Brenner [9] and Jeffery [22]. Several semi-empirical formulas for the drag force on a sphere have been published over the years, of which the simple expression by Schiller and Naumann [37] is among the most popular. The Schiller-Naumann correlation is known to provide an accurate drag force up to $Re_p \approx 800$. Motivated by the need also for extensions of the force and torque expressions for spheroids to finite Reynolds numbers, some alternative formulas have been proposed during the last decade. These formulas were primarily obtained by curve-fitting to computed forces and torques, notably by Hölzer and Sommerfeld [20], [21], Zastawny et al. [50] and Ouchene et al. [32].

Hölzer and Sommerfeld [20] developed their correlation formula for the drag coefficient using a large number of experimental data from the available literature, together with results from their in-house Lattice-Boltzmann simulations [21]. They claim that their correlation is reliable for the entire range of subcritical Reynolds numbers. Zastawny et al. [50] derived formulas for drag, lift and torque coefficients, which were validated by means of individual numerical solutions of the Navier-Stokes equation using an IB method to represent a nonspherical particle. Ouchene et al. [32] came up with a new set of correlation formulas for drag, lift and torque coefficients. Their correlations were based on in-house computational results [31] obtained with a body-fitted Navier-Stokes solver covering Reynolds numbers Re_p over the range from 0.1 to 290.

Sanjeevi and Padding [35] explored the orientation dependence of drag on spheroids over a fairly large range of Reynolds numbers and subsequently presented new correlation formulas (Sanjeevi et al. [36]). In an earlier paper by Jiang et al. [23] we showed computed results for drag, lift and torques for a 6:1 prolate spheroid at 45 ° attack at $Re = 50$ and compared with the Hölzer and Sommerfeld [20] and Zastawny et al. [50] correlations. Such force- and torque-correlations have recently been used in simulations of turbulent channel flow by van Wachem et al. [46], Tavakol et al. [44] and Arcen et al. [3].

1.4 Present contribution

The aim of the present work is to examine the three-dimensional flow field around a prolate spheroid at low but finite Reynolds numbers and at some different attack angles. A comprehensive coverage of the three-dimensional parameter space (aspect ratio, attack angle and Re) will not be undertaken. Accordingly, to provide new correlation formulas for the forces and torques on the spheroid is beyond our scope. The actual flow configuration and its parametrization is introduced in §2. The anticipated need for

unusually large computational domains and the unexpectedly high resolution requirements for Re < 1 are addressed in §3. Results obtained by accurately integrating the full Navier-Stokes equations will be presented §4. Drag and lift coefficients will be compared with finite-Re correlations derived by others (see §1.3) and with analytical results in the creeping-flow limit.

2. Computational modelling

2.1 Flow configuration

In this study, we simulate the flow field around a prolate spheroid with aspect ratio $\lambda = c/a = 6{:}1$, where $2c$ and $2a$ are the length of the major and minor axes, respectively. The Reynolds number is defined in terms of the uniform inflow velocity U_0 and the length of the minor axis $D = 2a$, i.e. $Re_D = U_0 D / \upsilon$, where υ is the kinematic fluid viscosity. Alternative Reynolds numbers can be based on a different reference length scale, for instance the volume-equivalent sphere diameter d. This Reynolds number, Re_P, is frequently used in studies of non-spherical particles; e.g. Ouchene et al. [31] and Sanjeevi and Padding [35]. For the case of a 6:1 prolate spheroid, $d = 1.817D$ and therefore $Re_P = 1.817 Re_D$.

The spheroid is inclined an angle θ in the (x, y)-plane, i.e. with respect to the inflow direction; see Figure 1. Five different incidence angles will be considered, *i.e.* $\theta = 0°, 22.5°, 45°, 67.5°,$ and $90°$ for two different Reynolds numbers $Re_D = 1$ and 10. In addition, the flow around spheroids at $Re_D = 0.1$ is simulated for three different attack angles and with different grid resolutions. Table 1 provides an overview of the different simulations.
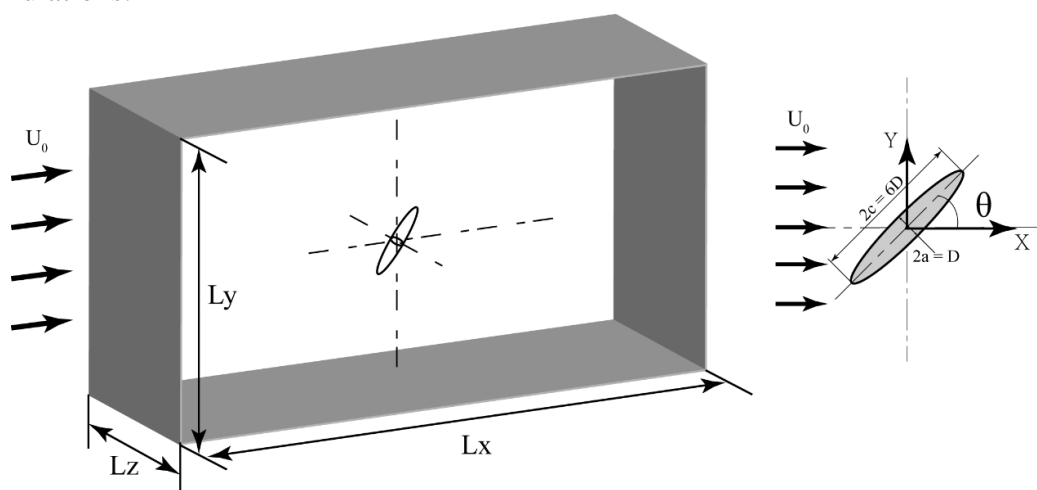
Figure 1. Schematic of the flow configuration. The 3D computational domain (not to scale) is shown to the left and the 6:1 prolate spheroid is detailed to the right. The origin of the Cartesian coordinate system is at the center of the spheroid. The incoming flow with uniform velocity U_0 is in the positive X-direction, with which the spheroid is inclined an angle θ.

5

Table 1. Physical and numerical parameters of the 17 different simulations. These cover 13 different flow configurations parameterized by Re_D and θ. Three different grid resolutions (c – coarse; m – medium; f – fine) are used for $Re_D = 0.1$.

Case	Re_D	Re_p	θ	Min grid size Δ/D	Total number of grid points $N_T \cdot 10^{-6}$
Re0.1-0-c	0.1	0.1817	0º	0.04	26.0
Re0.1-45-c	0.1	0.1817	45º	0.04	31.0
Re0.1-90-c	0.1	0.1817	90º	0.04	26.0
Re0.1-0-m	0.1	0.1817	0º	0.02	184.0
Re0.1-0-f	0.1	0.1817	0º	0.01	425.0
Re0.1-45-f	0.1	0.1817	45º	0.01	394.0
Re0.1-90-f	0.1	0.1817	90º	0.01	425.0
Re1-0	1	1.817	0º	0.04	26.0
Re1-22.5	1	1.817	22.5º	0.04	25.5
Re1-45	1	1.817	45º	0.04	31.0
Re1-67.5	1	1.817	67.5º	0.04	25.5
Re1-90	1	1.817	90º	0.04	26.0
Re10-0	10	18.17	0º	0.04	26.0
Re10-22.5	10	18.17	22.5º	0.04	25.5
Re10-45	10	18.17	45º	0.04	31.0
Re10-67.5	10	18.17	67.5º	0.04	25.5
Re10-90	10	18.17	90º	0.04	26.0

2.2 Mathematical modelling and numerical method

The steady three-dimensional (3D) flow field is governed by the mass conservation and the Navier-Stokes equation for unsteady flow of an incompressible Newtonian fluid:

$$\frac{\partial u_i}{\partial x_i} = 0 \tag{1}$$

$$\frac{\partial u_i}{\partial t} + u_j \frac{\partial u_i}{\partial x_j} = -\frac{1}{\rho}\frac{\partial p}{\partial x_i} + \upsilon \frac{\partial^2 u_i}{\partial x_j \partial x_j} \ . \tag{2}$$

These equations are discretized by a second-order finite-volume scheme on a staggered Cartesian grid using the Navier-Stokes solver MGLET due to Manhart et al. [27]. The initial flow field is marched forward in time by means of the explicit third-order Runge-Kutta scheme by Williamson [48] until a steady-state solution has been reached. The direct-forcing immersed boundary (IB) method developed by Peller *et al.* [33] is utilized to adapt the surface of the spheroid to the Cartesian grid. Local grid refinement is used to enable small grid cells in the vicinity of the spheroid whereas the grid is coarsened towards the boundaries of the computational domain. The local refinement is achieved by means of a multi-level hierarchy, as illustrated in Figure 2. The same

computational code was employed in our earlier studies of flow around a 45°inclined spheroid at higher Reynolds numbers, as reported by Jiang et al. [23], [24] and summarized by Andersson et al. [2].

2.3 Primary and secondary force- and moment-coefficients
Besides streamline plots aimed to illustrate the qualitative features of the computed flow fields, quantitative results will be provided in terms of the *primary* force and moment coefficients:

$$C_D = \frac{Drag}{\frac{1}{2}\rho U_0^2 \frac{\pi}{4} d^2} \tag{3}$$

$$C_L = \frac{Lift}{\frac{1}{2}\rho U_0^2 \frac{\pi}{4} d^2} \tag{4}$$

$$C_M = \frac{Torque}{\frac{1}{2}\rho U_0^2 \frac{\pi}{8} d^3}. \tag{5}$$

We refer to these coefficients as primary since the spanwise force component F_z and the streamwise and cross-stream moments M_x and M_y are zero due to the symmetry of the 3D-flow field about the (x, y)-plane at $z/D = 0$. This symmetry is first broken at Reynolds numbers way above the range considered herein, as shown by Jiang et al. [23], [24]. If also the *secondary* force and torque coefficients C_{Fz}, C_{Mx} and C_{My} are computed from a simulated flow field, they are expected to attain vanishingly small values.
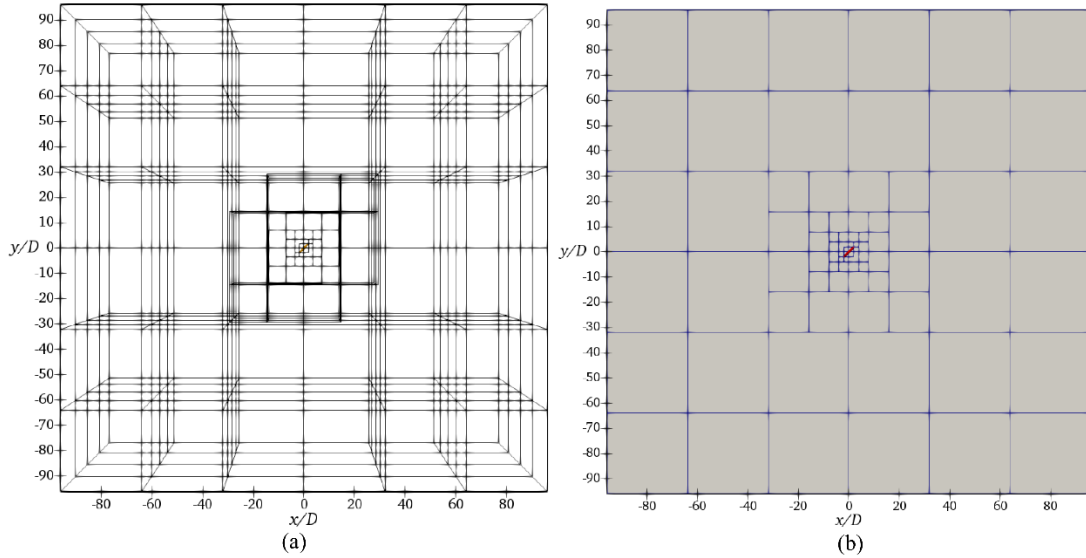
Figure 2. Illustration of the mesh structure used in the simulations for $\theta = 45°$. (a) The 3D mesh structure; (b) a 2D mesh slice in the symmetry plane, i.e. the (x, y)-plane at $z/D = 0$. Each cube shown in (a) contains $50 \times 50 \times 50 = 1.25 \times 10^5$ grid points. The size of the cubes in (a) and the squares in (b) reflects the resolution.

In the Stokes-flow limit $Re_D \rightarrow 0$, the analytical results derived by Brenner [9] will be used for comparisons. For a prolate spheroid inclined with respect to the oncoming flow, as in Figure 1, the drag and lift forces are:

7

$$Drag \,=\, \mu U_0[(K_{zz} - K_{xx})cos^2\theta + K_{xx}] \qquad (6)$$

$$Lift \,=\, -\mu U_0[(K_{xx} - K_{zz})sin\theta cos\theta\,]. \qquad (7)$$

The only non-zero components of the resistance tensor K_{ij} in a coordinate frame aligned with the major (z) and minor (x) axes of a prolate spheroid are given for instance by Gallily and Cohen [18] and Siewert et al. [41]:

$$K_{xx} = 16\frac{\pi a^2 c}{\chi + a^2\alpha} \;\; ; \;\; K_{zz} = 16\frac{\pi a^2 c}{\chi + a^2\gamma}, \qquad (8)$$

where

$$\chi = -\frac{a^2\lambda}{\sqrt{\lambda^2-1}}\kappa \qquad (9)$$

and α and γ are dimensionless shape factors:

$$\alpha = \frac{\lambda^2}{\lambda^2-1} + \frac{\lambda}{2(\lambda^2-1)^{3/2}}\kappa; \;\; \gamma = -\frac{2}{\lambda^2-1} - \frac{\lambda}{(\lambda^2-1)^{3/2}}\kappa\,; \qquad (10)$$

$$\kappa = \ln(\frac{\lambda-\sqrt{\lambda^2-1}}{\lambda+\sqrt{\lambda^2-1}})\,. \qquad (11)$$

For the 6:1 spheroid, the resistance components become $K_{xx} = 25.20D$ and $K_{zz} = 18.53D$.

3. Computational challenges for low-Re simulations

The Reynolds number Re_D measures the relative importance of inertia and viscous forces. While viscous effects are confined to thin boundary layers when $Re_D \gg 1$, viscous stresses will influence the flow field far away from the spheroid for $Re_D \ll 1$ and all the way to infinity in the creeping-flow or Stokes limit $Re_D = 0$. It can therefore be anticipated that unusually wide computational domains are required for low-Re simulations, *i.e.* large cross-sections $L_y \times L_z$ in Figure 1. On the other hand, the generally large velocity gradients in the vicinity of the spheroid will reduce with decreasing Re_D and the grid resolution requirements are therefore expected to be relieved. An overview of related investigations are provided in the accompanying Table 2.

In this section we first examine the need for a wide domain at the lowest Reynolds number $Re_D = 0.1$ considered in this study. We thereafter address the grid resolution requirements at the same low Reynolds number.

3.1 Size of the computational domain for $Re_D = 0.1$

In our previous study (Jiang *et al.* [23]) of laminar flow around a 6:1 prolate spheroid, a grid refinement test showed that a minimum grid size $\Delta = 0.04D$ was adequate for the simulation at $Re_D = 50$. In view of the lower Reynolds numbers considered in the present work, i.e. $Re_D \leq 10$, we adopt the same Δ for most of the simulations herein (see Table 1), anticipating that the grid requirement is relieved for lower-Re flows.

Table 2. Overview of recent computations of flow past prolate spheroids. Some of these studies include also other geometrical shapes than prolate spheroids. The Reynolds number ranges are in most of the other studies based on Re_p rather than on Re_D.

Authors	Year	Re	Aspect Ratio λ	Method	Domain $L_y \times L_z$	Boundary Conditions
Hölzer & Sommerfeld[21]	2009	0.3 - 240	3:2	LB	74 ×60	symmetry
Richter & Nikrityuk [34]	2012	10 – 250	2:1	body-fitted finite-volume	20 ×20	symmetry
Zastawny et al.[50]	2012	0.1 – 300	5:4; 5:2	IB	20 ×20	free-slip
Ouchene et al. [31]	2015	0.1 - 290	5:4; 5:2; 5:1	body-fitted finite-volume	80 ×80	no-slip
Sanjeevi et al. [36]	2018	0.1 – 2000	5:2	LB	20 ×20	free-slip
Present study	2018	0.1 - 10	6:1	IB	192 ×128	free-slip
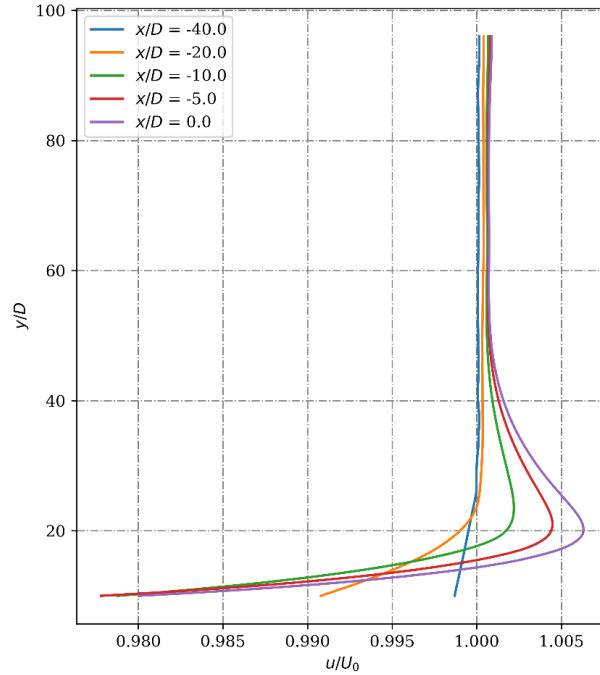
Figure 3. Streamwise velocity profile u/U_0 in the geometrical symmetry plane ($z/D = 0$) at $x/D = -40$, -20, -10, -5, and 0. Attack angle $\theta = 0°$ and Reynolds number $Re_D = 0.1$. Domain size $192D \times 192D \times 128D$. The profiles are plotted for $y/D \geq 10$.

A challenge in CFD at low Reynolds numbers is that viscous effects are spreading far away from the spheroidal body. The common usage of free-slip boundary conditions on the sides of the computational domain, *i.e.* Neumann conditions on the tangential velocity components and a Dirichlet condition on the normal velocity component, cannot be justified unless the cross-section of the computational domain is unusually large.

In the present study, the same free-slip boundary conditions as those used by Jiang et al. [23] are imposed at the four sides of the computational domain depicted in Figure 1. To illustrate the far-reaching viscous effects at $Re_D = 0.1$, we first computed the flow field when the major axis of the 6:1 spheroid was aligned with the oncoming flow, i.e. in the x-direction. Velocity profiles $u(y)$ at some different locations upstream of the spheroid are shown in Figure 3. The streamwise velocity component u varies symmetrically about $y = 0$, but only results above $y = 10D$ are shown here. $40D$ upstream of the center of the spheroid the velocity u approaches U_0 about $40D$ above the x-axis. Closer to the spheroid, at $x/D = -10$ and -5, the streamwise velocity exhibits a modest overshoot around $20D$ above the x-axis, before u decays to a constant level slightly above U_0 some $50D$ away from the x-axis. The largest overshoot, about 0.6% of U_0, is seen just above the mid-section of the spheroid ($x/D = 0$). These results suggest that a domain height $L_y = 100D$ would suffice at this particular Reynolds number ($Re_D = 0.1$) and at this angle of attack ($\theta = 0°$). Since the prolate spheroid is aligned with the flow direction in this particular test simulation, the flow field is symmetric about the x-axis. This suggests the proper domain width also to be at least $L_z = 100D$.

In order to explore the anticipated increasing domain-size effect at low Reynolds numbers, a domain-size study is performed at the lowest Reynolds number considered in the present work, namely $Re_D = 0.1$. The attack angle is hereinafter $45°$, and the smallest grid size is $\Delta = 0.04D$. The outcome of these test simulations is reported in Table 3 in terms of the primary force and moment coefficients defined in Section 2.3.

Table 3. Overview of test cases for a 6:1 spheroid at 45° angle of attack and $Re_D = 0.1$ and smallest grid size $\Delta = 0.04D$.

Case	Domain size $(L_x/D \times L_y/D \times L_z/D)$	La = $\sqrt[3]{L_x L_y L_z}$	C_D	- C_L	C_M
A1	$28 \times 32 \times 11$	21.44	210.34	38.65	11.34
A2	$40 \times 32 \times 20$	29.47	194.78	34.27	6.10
A3	$80 \times 50 \times 40$	54.29	182.34	33.71	5.87
A4	$160 \times 160 \times 96$	134.95	163.25	32.22	5.52
A5	$192 \times 192 \times 128$	167.73	163.11	32.15	5.51

Starting from the same size of the computational domain as that used by Jiang et al. [23] for $Re_D = 50$, the domain size was gradually increased in all three directions. We use the size La of a volume-equivalent cube as a measure of the domain size. La increased from $21D$ for Case A1 to $167D$ for Case A5. The resulting force and moment

coefficients exhibit a surprisingly strong dependency on the size of the computational domain. All coefficients show a decreasing dependence on La and the moment coefficient C_M is reduced by 50% from the smallest to the largest domain. Fortunately, the computed values of the coefficients seem to converge. A similar decaying trend was observed for a 5:2 spheroid by Sanjeevi et al. [36]. The deviations between our Case A4 and Case A5 are negligibly small and we safely conclude that the domain size $L_x/D \times L_y/D \times L_z/D = 192 \times 192 \times 128$ is suitable for all simulations to be undertaken in the present study (to be reported in Section 4). Since we are concerned with the flow around an inclined spheroid, we intentionally chose the domain height larger than the domain width, *i.e.* $L_y > L_z$. This is consistent with the choice made by Hölzer and Sommerfeld [21]; see Table 2.

We have now learned that computer simulations at Reynolds numbers below unity are exceptionally demanding with respect to the size of the computational domain. Even with cross-section $L_y \times L_z = 50D \times 40D$ (Case A3), the drag coefficient C_D is over-predicted by more than 10%. This is because the viscous stresses are not only effective inside a thin boundary layer, as for $Re_D \gg 1$, but diffuse the effect of the spheroid surprisingly far away from the body itself. The present findings are supported by figure 10 in Sanjeevi et al. [36] for $Re_p = 0.1$, from which one observe that the wider domain used by Ouchene et al. [31] gives much better results than the correlation proposed by Zastawny et al. [50].

3.2 Grid resolution study for $Re_D = 0.1$

The required grid resolution is normally dictated by spatial gradients of the flow variables to be solved for, e.g. u_i and p in equations (1) and (2). The velocity component along a solid surface varies rapidly from no-slip at the surface and approaches the free-stream velocity U_0 away from the surface at high Reynolds numbers. However, such a thin boundary layer does no longer exist for Reynolds numbers of the order of unity. Instead, the adaption of the velocity u to U_0 takes place over a fairly long distance, as shown in Figure 3. One might therefore be inclined to infer that a fine grid is no longer needed for low-Re simulations. However, although the IB-method gives reliable results for the three-dimensional flow field, an imperfect representation of a curved surface in a Cartesian mesh reduces the accuracy in the immediate vicinity of the originally smooth surface.

Table 4. Force coefficients for $Re_D = 0.1$ obtained with three different grid resolutions (c – coarse; m – medium; f – fine) at three different attack angles θ.

Case	θ	Δ/D	C_D	Theory C_D	Deviation*	$|C_L|$	Theory $|C_L|$	Deviation*
Re0.1-0-c	0°	0.04	122.17	142.91	-14.5%	4.3E-4	0	NA
Re0.1-0-m	0°	0.02	134.52	142.91	-5.9%	3.5E-4	0	NA
Re0.1-0-f	0°	0.01	138.39	142.91	-3.2%	2.1E-4	0	NA
Re0.1-45-c	45°	0.04	163.11	168.64	-3.3%	32.15	25.74	24.9%

Re0.1-45-f	45°	0.01	174.22	168.64	3.3%	28.39	25.74	10.3%
Re0.1-90-c	90°	0.04	193.30	194.38	-0.6%	1.1E-3	0	NA
Re0.1-90-f	90°	0.01	203.44	194.38	4.7%	6.2E-4	0	NA

*deviation = 100% $\times (C_D(\text{simulation}) - C_D(\text{theory})) / C_D(\text{theory})$

With the view to examine the effect of the grid resolution next to the spheroid, we performed simulations with three different grid resolutions at $Re_D = 0.1$. The results for the drag and lift coefficients are provided in Table 4. In view of the very low Reynolds number, the computed coefficients should be comparable with the theoretical solutions (6), (7), which are formally valid only for $Re_D = 0$. The data reported in Table 4 show that the drag coefficient C_D increases as the size Δ of the smallest grid spacing, which is found in the innermost cubes in Figure 2, is reduced from $0.04D$ to $0.01D$. We believe that the unexpectedly large (14.5%) under-prediction of C_D on the coarsest grid (*c*) is primarily due to imperfections of the IB-representation of the surface of the spheroid. According to Stokes' theory, the viscous contribution is exactly twice the pressure contribution to the drag force on a spherical body. The viscous contribution to C_D is substantially higher for a prolate spheroid aligned in the flow direction, as shown by Ouchene et al. [31]. Since an imperfect boundary representation affects the viscous surface stress but not the surface pressure, the unexpectedly high resolution requirement is of primary concern whenever the drag force is dominated by viscous stresses, i.e. for $\theta = 0^\circ$. With the finest grid (*f*), the computed drag coefficients in Table 4 are all within 5% of the theoretical values given by equation (6) for aligned, inclined, and normally oriented spheroids.

The observation that the drag coefficient approaches its theoretical value as the grid is refined is observed only when the spheroid is aligned with the flow, i.e. for $\theta = 0^\circ$. A major fraction of the overall drag stems from viscous forces, which are predicted accurately only on a fine mesh. At large angles of attack, however, pressure makes a substantial contribution to C_D, which therefore becomes less sensitive to grid resolution.

The entries for the lift coefficient in Table 4 are vanishingly small for the spheroid aligned with the flow ($\theta = 0^\circ$) and for a perpendicularly oriented spheroid ($\theta = 90^\circ$). Indeed, both these orientations result in a flow field which is symmetric about the (x, z)-plane at $y = 0$. However, when the spheroid is inclined 45°, the lift coefficient becomes significant, albeit only less than 20% of C_D. On the finest mesh (*f*), the magnitude of C_L is about 10% over-predicted as compared with the asymptotic solution in equation (7). According to computations by Ouchene et al. [31], the pressure field contributes more than the viscous stresses to the lift force.

We speculate that the results for the force coefficients can be further improved if an even finer mesh resolution could be used in the vicinity of the spheroid so that any surface imperfections can be further reduced. However, the total number of grid points are already of the order of 400 million for the finest mesh (see Table 1), partly because of the domain size requirements addressed in the preceding sub-section. A further grid refinement will also affect the stability of the explicit time-marching scheme (3rd-order

Runge-Kutta). The conventional CFL-condition is easily satisfied in wake-flow simulations at high Reynolds numbers. For $Re_D < 1$, however, another stability condition assures that momentum should never diffuse over more than one grid cell Δx per time step Δt. A formal derivation of this condition for a general three-dimensional case is not at all straightforward, see for instance Beckers [8]. For the wake flow simulation at $Re_D = 0.1$ and $\theta = 0^o$, we realized that $\Delta t \sim (\Delta x)^4$ which makes a refined grid simulation even more demanding than suggested by the increasing number of grid points.

Computations of flow around a prolate spheroid at $Re_D = 0.1$ using an IB-method require not only a huge computational domain, but also an unexpectedly fine grid in the vicinity of spheroid. Both are low-Reynolds number challenges which are gradually relieved at the higher $Re_D = 1$ and 10. This conjecture was verified by means of a test simulation at $Re_D = 1$ and $\theta = 0^o$, but with a refined mesh $\Delta/D = 0.02$ rather than $\Delta/D = 0.04$ used in Case *Re1-0*. The primary force and moment coefficients compared with those in Table 5 to within 0.5%. While the domain size requirement is universal, the grid size requirement is associated with the IB-method. A recent remedy to enhance the accuracy in the vicinity of the surface is higher-order reconstructions of near-surface velocities (Xia et al. [49]).

4 Results and discussions

Selected results from the computations of the different flow configurations introduced in Section 2.1 are presented in the following sub-sections. All simulations reported herein used the largest $192D \times 192D \times 128D$ domain size. Streamlines in the meridional and the equatorial planes are first presented in Section 4.1 for some representative values of attack angle θ and Reynolds number Re_D, followed by computed values of the force, lift and torque coefficients in Section 4.2. The latter data are compared with correlation formulas proposed by Hölzer & Sommerfeld [20] and Ouchene et al. [32] in Section 4.3.
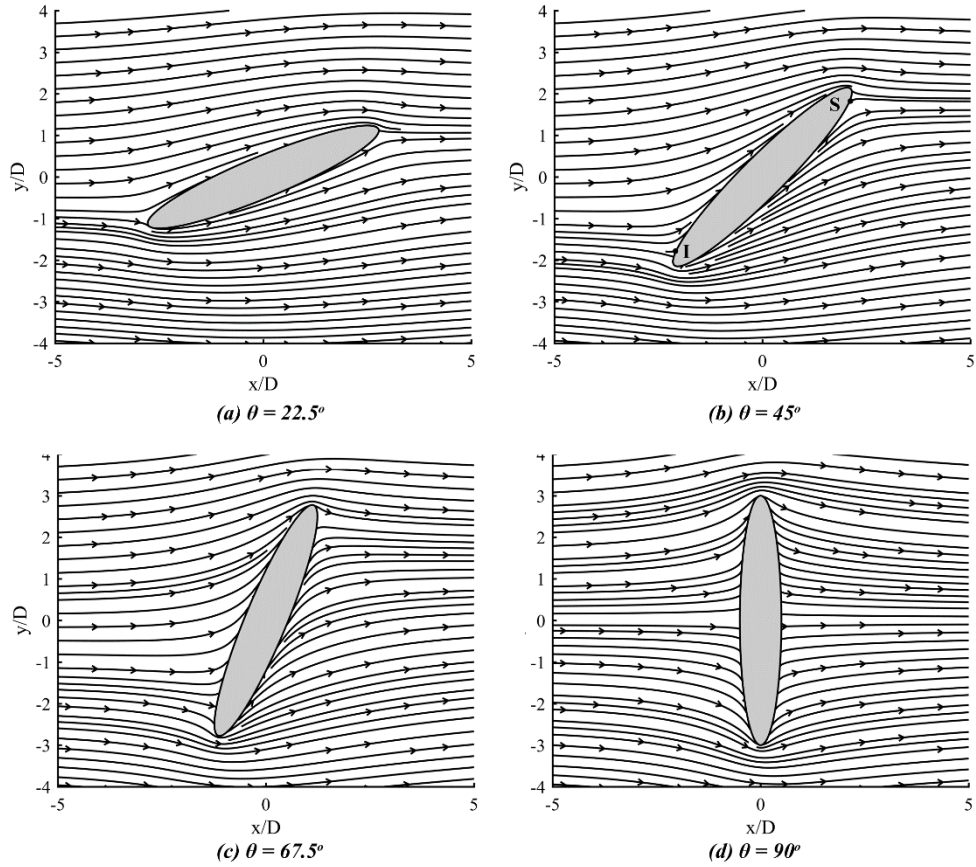
Figure 4. Streamlines in the meridional plane for four different attack angles for $Re_D = 1$. The impingement point (I) and the separation point (S) are indicated in panel (b).

4.1 Three-dimensional flow fields

Only low-Reynolds-number flows are considered in this paper, for which the flow around the inclined prolate spheroid is steady and symmetric about the geometrical mid-plane, i.e. about $z/D = 0$. The equatorial plane, *i.e.* the plane through the mass center of the spheroid and with unit normal aligned with its symmetry axis, is a plane of symmetry of the spheroidal body. However, the equatorial plane is a plane of symmetry of the flow field only if the spheroid is aligned perpendicular to the inflow (at 90° angle of attack).

14
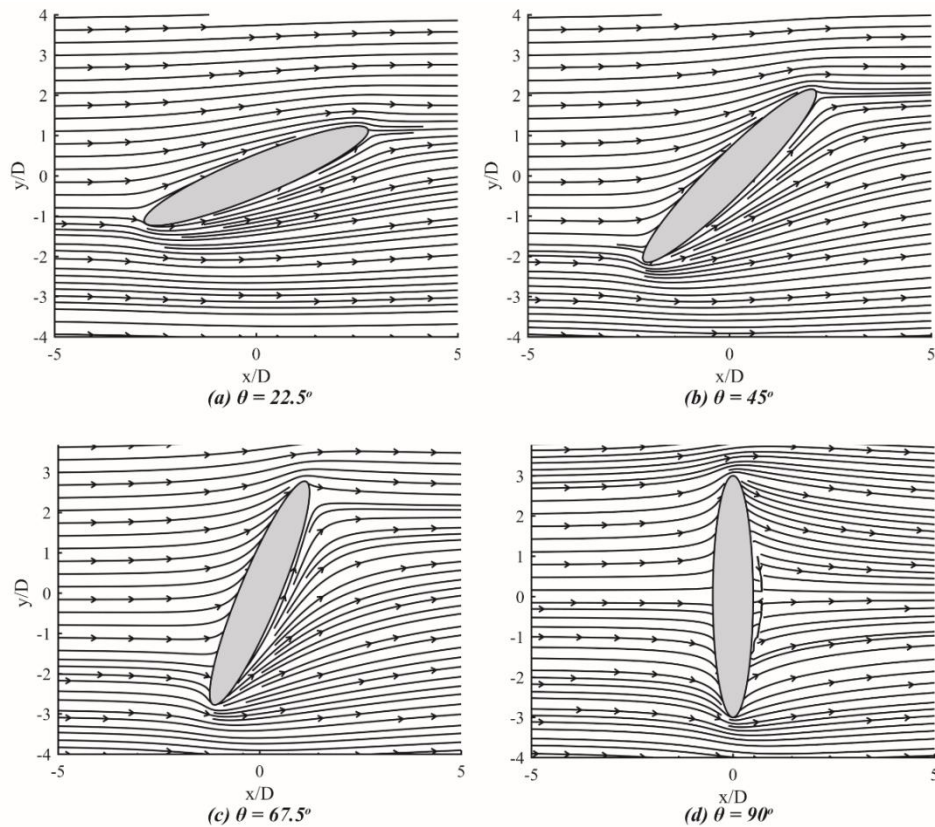
**Figure 5**. Streamlines in the meridional plane for four different attack angles for $Re_D = 10$.

4.1.1 Streamlines in the meridional plane

Streamlines in the meridional plane (the geometrical symmetry plane at $z/D = 0$) are shown in Figure 4 for $Re_D = 1$ and in Figure 5 for $Re_D = 10$. The effect of the two different Reynolds numbers is best seen in the bulging of the streamlines above and below the spheroid. The streamlines at $y/D = \pm 4$ reveal that the flow is much better aligned in the streamwise x-direction for $Re_D = 10$ than for the lower Reynolds number. At $45°$ attack, the flow impinges near the leading pole of the spheroid. The flow is directed along both sides of the spheroid until the flow along the rear side separates from the curved surface close to the upper pole, see for instance Figure 5b. The separation point (S) is located almost anti-symmetrically of the impingement point (I) at these fairly low but yet finite Reynolds numbers. A perfect fore-aft symmetry is expected only at $Re_D = 0$.

4.1.2 Streamlines in the equatorial plane

Streamlines in the equatorial plane are shown in Figure 6 for some different attack angles for $Re_D = 10$. Contrary to the streamlines in Figures 4 and 5, the lines shown in Figure 6 are not true streamlines but rather lines through projections of the three-

dimensional velocity vectors into the plane. Except for the perpendicularly oriented spheroid ($\theta = 90°$), a substantial flow through the equatorial plane is present.

(a) θ = 22.5°   *(b) θ = 45°*

(c) θ = 67.5°   *(d) θ = 90°*
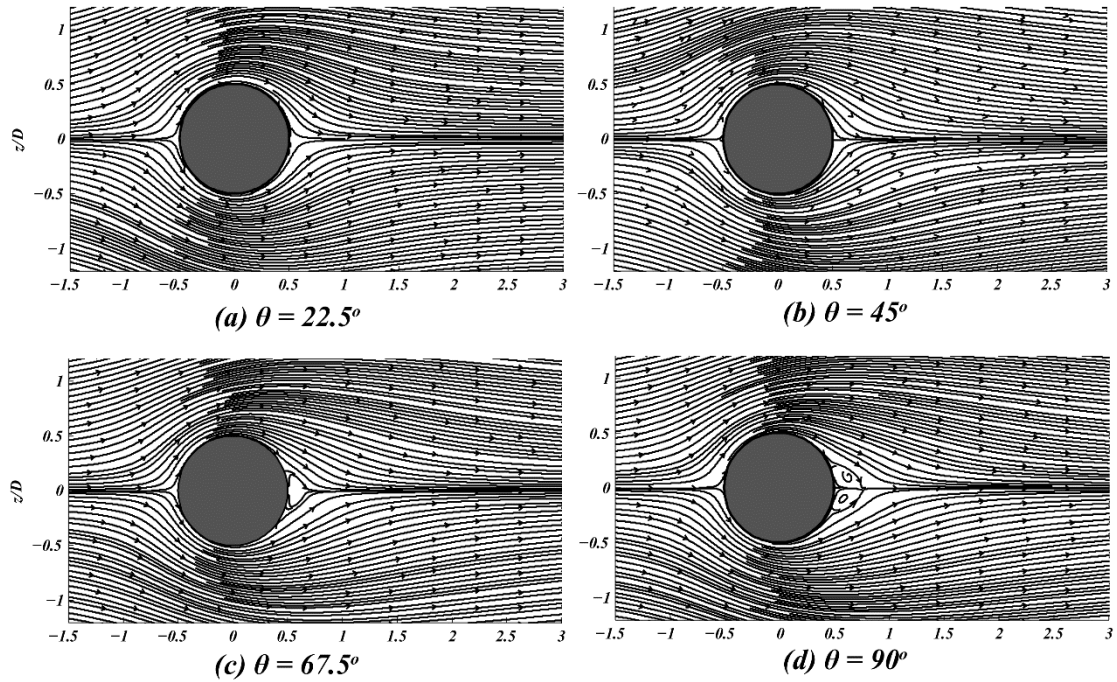
Figure 6. Streamlines in the equatorial plane for four different attack angles for $Re_D = 10$. The equatorial plane is the plane perpendicular to the symmetry axis of the spheroid through its mass center.

A modest fore-aft asymmetry can be observed at low angles of attack in Figure 6a, b. This asymmetry seems to increase with increasing angle of attack. The streamlines at $\theta = 67.5°$ suggest that the flow is on the verge to separate from the surface of the spheroid and the streamlines at $\theta = 90°$ reveal a pair of zones of recirculating flow.

The tendency of the flow to separate from the spheroid is clearly a Reynolds number dependent phenomenon, as shown in Figure 7. The streamlines at the lower Reynolds number $Re_D = 1$ show an attached flow all the way to the rear of the spheroid, contrary to the separated flow at $Re_D = 10$. The flow topology in the equatorial plane resembles the two-dimensional flow field around an infinitely long circular cylinder at a Reynolds number around unity. The visualized streamline pattern at $Re_D = 1.54$ in Van Dyke [45] is clearly in between those in panels (a) and (b) of Figure 7.
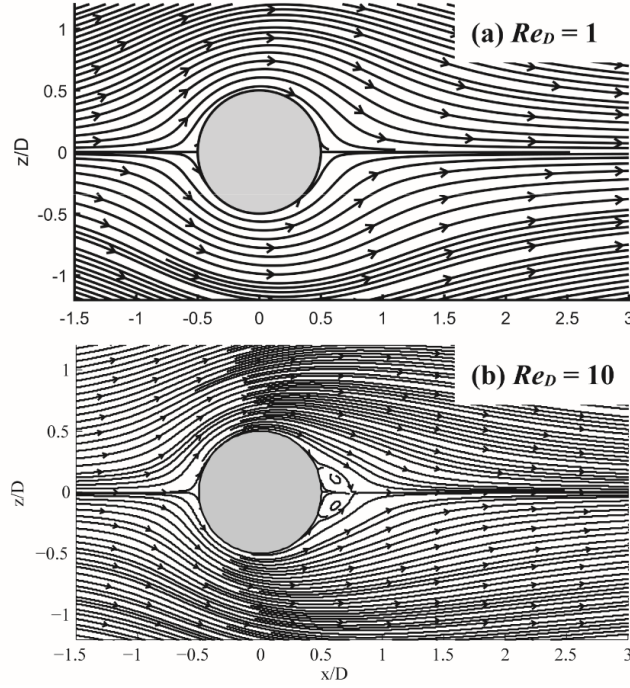
Figure 7. Streamlines in the equatorial plane for attack angle $\theta = 90^\circ$ for (a) $Re_D = 1$ and (b) $Re_D = 10$.

Table 5. Compilation of all force and moment coefficients for all Re_D and θ. All simulations are with the largest domain size ($192D \times 192D \times 128D$). The mesh resolution for the various cases is given in Table 1.

Case	Re_D	θ	C_D	$|C_L|$	C_{Fz}	C_{Mx}	C_{My}	C_M
Re0.1-0-f	0.1	0°	138.39	2.1E-04	8.1E-04	-2.4E-04	-9.8E-05	-3.3E-04
Re0.1-45-f	0.1	45°	174.22	28.39	2.3E-03	1.5E-04	-5.9E-04	5.24
Re0.1-90-f	0.1	90°	203.44	6.2E-04	-4.9E-04	8.6E-05	1.4E-04	-5.8E-05
Re1-0	1	0°	14.98	2.3E-04	-2.7E-04	9.3E-05	-2.0E-04	-9.3E-05
Re1-22.5	1	22.5°	16.82	3.07	3.1E-04	3.4E-04	-5.1E-03	2.51
Re1-45	1	45°	19.26	4.43	-4.6E-04	3.1E-04	6.7E-03	3.65
Re1-67.5	1	67.5°	22.87	3.27	-6.9E-04	-5.9E-04	-3.4E-03	2.55
Re1-90	1	90°	24.40	1.9E-04	-7.7E-05	-3.8E-04	-4.1E-05	6.8E-04
Re10-0	10	0°	2.12	1.2E-05	1.4E-05	1.4E-05	-1.0E-05	7.6E-06
Re10-22.5	10	22.5°	2.54	0.70	-7.7E-05	2.5E-05	-7.6E-04	1.07
Re10-45	10	45°	3.59	1.12	-3.9E-04	1.7E-05	-8.5E-04	1.52
Re10-67.5	10	67.5°	4.70	0.87	-5.4E-04	-4.2E-05	-5.9E-04	1.08
Re10-90	10	90°	5.17	1.5E-05	3.9E-06	6.8E-05	-8.5E-06	3.2E-05

4.2 Drag, lift and moment coefficients

The computed force and torque coefficients are summarized in Table 5. In addition to the primary coefficients defined in equations (3)-(5), we also include the similarly defined secondary coefficients C_{Fz}, C_{Mx}, and C_{My}. The latter coefficients are formally

zero as long as the wake retains its symmetry about the meridional plane. It is readily observed from the entries in Table 5 that the computed values of these coefficients are lower than the primary coefficients by a factor of 0.001 or more. The vanishingly low values of the secondary coefficients serve as an additional validation of the computed flow fields. This is, however, not the case for $Re_D = 3000$, for which a severely skewed wake was observed behind the $\theta = 45\,°$ inclined 6:1 spheroid by Jiang et al. [24]. This distinctly asymmetric wake gave rise to a substantial sideway force C_{Fz} as well as to secondary moments.

Inspection of Table 5 shows that the lift force and the spanwise moment vanish when the spheroid is either aligned in the flow direction ($\theta = 0\,°$) or perpendicular to it ($\theta = 90\,°$). This is a direct consequence of the symmetry of the streamlines about the (x, z)-plane in these cases, *e.g.* Figure 4(d) and 5(d). Accordingly, the only integrated effect from the viscous flow field on the spheroid is the drag force parameterized as C_D.

4.3 Comparison of computed coefficients with correlation formulas

The computed drag coefficients are provided in Table 6, together with corresponding values obtained from the correlation formulas provided by Hölzer and Sommerfeld [20] and Ouchene et al [32]. The correlation formulas of Zastawny et al. [50] involve shape-specific parameters and are therefore not applicable to higher aspect ratio particles. The deviations of the computed drag coefficient from the two correlation formulas are of the order of 10% and without any obvious tendencies, except for the larger deviations at $Re_D = 10$ and $\theta \geq 67.5°$.

In their recent paper, Sanjeevi et al. [36] made comparisons with the coefficients deduced from their LB method simulations at two significantly higher Reynols numbers $Re_p = 100$ and 2000. Their computed data were in good agreement with the correlation of Zastawny et al. [50], which is known to be inaccurate at lower Reynolds numbers. The more generic correlation of Ouchene et al. [32] was comparatively less accurate at these Reynolds numbers. In this sub-section, the results of the present simulations are compared with relevant correlations in the low-Re range $Re_D \leq 10$.
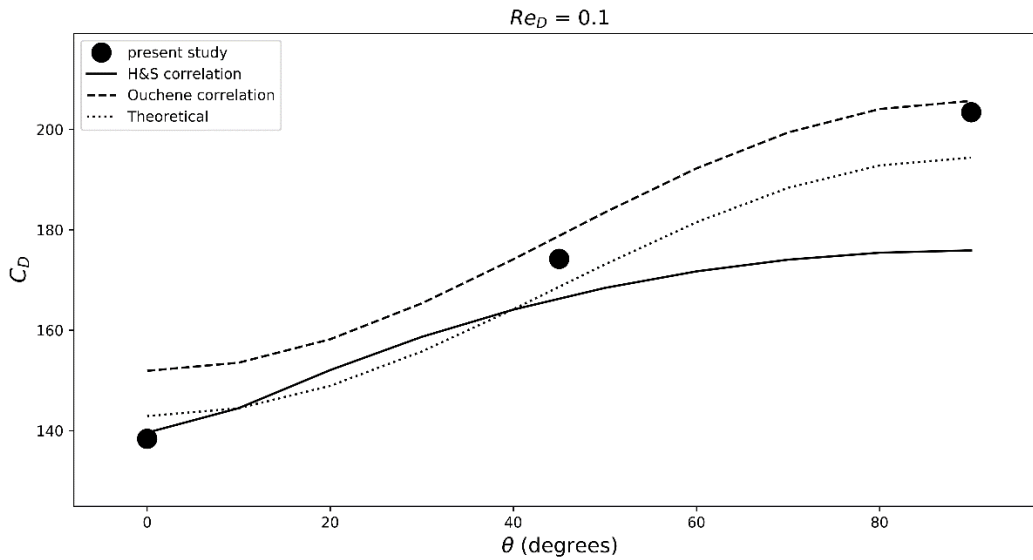
The variation of the drag coefficient C_D with attack angle θ is shown in Figure 8 for $Re_D = 0.1$ and in Figure 9 for $Re_D = 1$ and 10. At the lowest Reynolds number in Figure 8, it can be anticipated that the correctly computed drag coefficient should be only slightly higher than the theoretical C_D-value obtained from equation (6), which is formally valid only in the $Re_D = 0$ limit. This is not the case when the spheroid is aligned with the flow direction. The drag on a prolate spheroid with zero attack angle is dominated by viscous stresses at this low Reynolds number. The modest under-prediction of C_D is probably an effect of an insufficient surface representation by the IB method, as explored in Section 3.2. However, as the attack angle θ increases, the relative contribution of the viscous stresses is reduced whereas the pressure becomes gradually more important. The drag force on the spheroid when oriented perpendicular

to the free stream is slightly higher than the creeping-flow solution (6), as one should expect, and almost coincides with the Ouchene-correlation.

Table 6. Computed drag coefficients C_D compared with correlation formulas by Hölzer & Sommerfeld [20] and Ouchene et al. [32]. The latter formula has been corrected for some typos pointed out by Arcen et al. [3].

Case	Re_D	Re_p	θ	C_D	H & S	Deviation*	Ouchene et al.	Deviation*
Re0.1-0	0.1	0.1817	0°	138.39	139.58	-0.9%	151.91	-8.9%
Re0.1-45	0.1	0.1817	45°	174.22	166.4	4.7%	178.79	-2.6%
Re0.1-90	0.1	0.1817	90°	203.44	175.9	15.7%	205.68	-1.1%
Re1-0	1	1.817	0°	14.98	16.18	-7.4%	16.94	-11.6%
Re1-22.5	1	1.817	22.5°	16.82	17.92	-6.1%	18.06	-6.9%
Re1-45	1	1.817	45°	19.26	19.57	-1.6%	20.76	-7.2%
Re1-67.5	1	1.817	67.5°	22.87	20.55	11.3%	23.46	-2.5%
Re1-90	1	1.817	90°	24.40	20.88	16.9%	24.57	-0.69%
Re10-0	10	18.17	0°	2.12	2.47	-14.2%	2.27	-6.6%
Re10-22.5	10	18.17	22.5°	2.54	2.96	-14.2%	2.57	-1.2%
Re10-45	10	18.17	45°	3.59	3.51	2.3%	3.28	9.6%
Re10-67.5	10	18.17	67.5°	4.70	3.88	21.1%	3.99	17.8%
Re10-90	10	18.17	90°	5.17	4.01	28.9%	4.28	20.8%

*: deviation = 100% × (C_D(simulation) - C_D(correlation)) / C_D(correlation)

Figure 8. Variation of drag coefficient C_D with attack angle θ for $Re_D = 0.1$. Data from Table 6 are plotted together with the theoretical solution (6).

The attack angle dependence of C_D is also shown in Figure 9, but for higher Reynolds numbers. Aside from the substantially lower values at $Re_D = 10$ than at $Re_D = 1$, the drag coefficient is a monotonically increasing function of θ. It is noteworhty that the present data, as well as the Ouchene-correlation, exhibit an inflection point at both these Reynolds numbers. As expected, all results in Figure 9(a) are consistently above the results deduced from the analytical creeping flow solution (6). The drag coefficient for $\theta = 90°$ in Figure 9(b) is over-predicted by more than 20% compared to the two correlation formulas. This is obviously associated with the separated flow behind the spheroid seen in Figure 6(d), which inevitably increased the pressure drag.
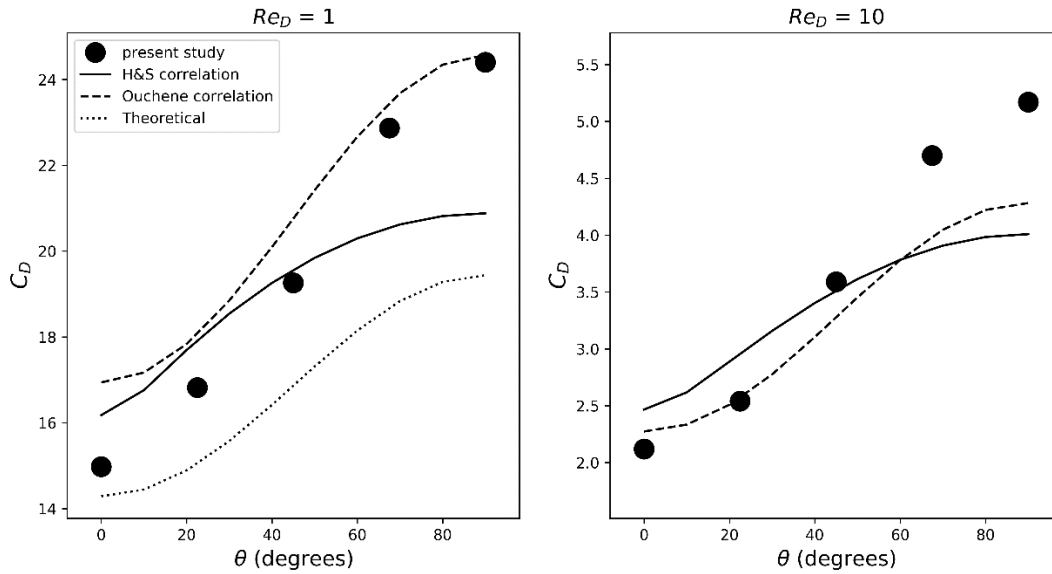
Figure 9. Variation of drag coefficient C_D with attack angle θ for $Re_D = 1$ (left) and $Re_D = 10$ (right) Data from Table 6. The theoretical solution (6) is included in the left panel.

Table 7. Computed lift C_L and torque C_M coefficients compared with correlations by Ouchene et al. [32] corrected for some typos pointed out by Arcen et al. [3]. Entries for $\theta = 0°$ and $90°$ are not included.

Case	C_L	Ouchene et al.	Deviation*	C_M	Ouchene et al.	Deviation*
Re0.1-45-f	28.39	20.05	41.6 %	5.24	4.50	16.4 %
Re1-22.5	3.069	2.547	20.5 %	2.507	1.35	85.7 %
Re1-45	4.427	3.61	22.6 %	3.646	1.91	90.9 %
Re1-67.5	3.270	2.56	27.7 %	2.546	1.35	88.6 %
Re10-22.5	0.702	0.542	29.5 %	1.070	0.66	62.1 %
Re10-45	1.119	0.784	42.7 %	1.520	0.94	61.7 %
Re10-67.5	0.874	0.56	56.1 %	1.080	0.66	63.6 %

*: deviation = 100% $\times$ (C(simulation) - C(correlation)) / C(correlation)

Finally, computed lift and moment coefficients (C_L and C_M) are compared with Ouchene et al. [32] correlations in Table 7 and in Figure 10. While the deviations

between the computed drag coefficient and the corresponding correlation formulas in Table 6 were of the order of 10%, the computed lift coefficients in Table 7 deviate by some 20 to 60 per cent and the moment coefficients deviate even more. The computed coefficients (circles and squares in Figure 10) are consistently over-predicted for all attack angles and at all Reynolds numbers considered. The largest overpredictions, about 90%, are for the moment coefficient at $Re_D = 10$ (Figure 10b).
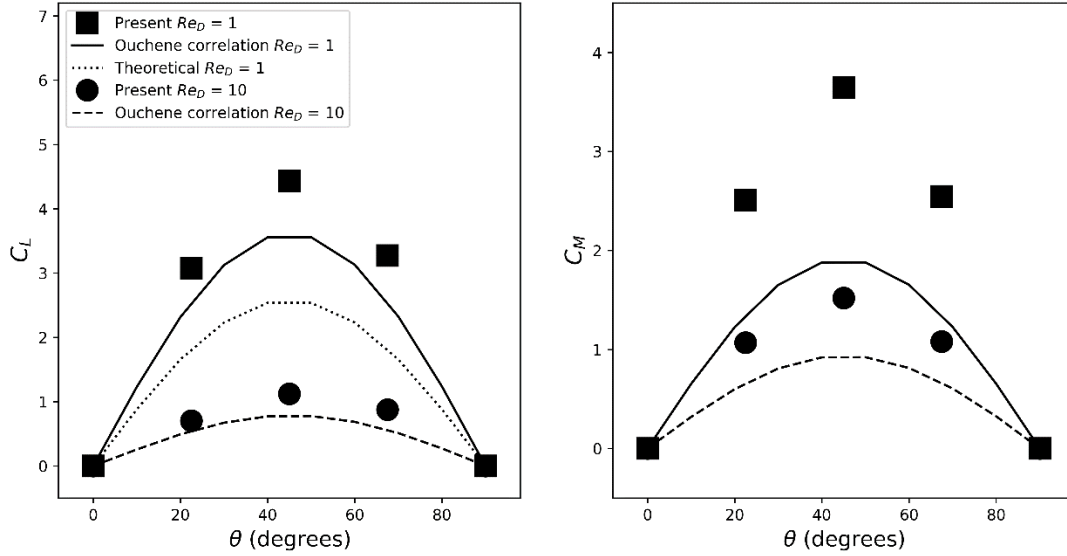
Figure 10. Lift and moment coefficients obtained from the present computations compared with the Ouchene-correlations [32] for $Re_D = 1$ and 10. (a) Lift coefficient C_L; (b) Moment coefficient C_M.

The present computations at $Re_D = 0.1$ and $\theta = 45°$ overpredicted C_D and C_L by only about 3% and 10%, respectively (see Table 4). The Ouchene-correlations [32] provide lift- and momentum-coefficients that deviated substantially from the present computations in the low-Re range $0.1 \leq Re_D \leq 10$. The deviations between the present computations and the Ouchene-correlation for C_L are equally large at $Re_D = 10$ as at $Re_D = 0.1$ and of the order of 40%, whereas even larger deviations are observed for C_M in Figure 10b. The size of the computational domain used by Ouchene et al. [31] is reasonably good; see Table 2. However, their use of no-slip rather than free-slip conditions might possibly affect their computations on which their correlation-formulas are based.

5. Concluding remarks

The three-dimensional flow field around a 45° inclined 6:1 prolate spheroid has been considered at low but finite Reynolds numbers. The need for exceptionally large computational domains has been explored. This was particularly challenging at the lowest Reynolds number $Re_D = 0.1$ considered since the viscous stresses are influential far away from the body for $Re \sim 1$ and affect the flow field all the way to infinity in the creeping-flow limit as $Re \to 0$. Another and unexpected challenge at low Reynolds

numbers, ascribed to the use of the immersed boundary (IB) method to represent the spheroid in a Cartesian mesh, is the severe grid resolution requirements. This challenge arises for parameter combinations for which the viscous stresses dominate over pressure, i.e. notably when the spheroid is aligned with the flow direction at $Re_D = 0.1$.

Comparisons with correlation formulas for drag, lift and moment coefficients suggest that computations of flow fields around spheroids at Reynold numbers of order unity are challenging and the accuracy of already existing formulas can hardly be assessed. The usage of such finite-Re correlation formulas in point-particle simulations is not necessarily superior to simulations using analytically derived expressions, although the latter is formally valid only in the limit as $Re \rightarrow 0$. The outcome of the present study suggests that existing correlation formulas are more reliable at Reynolds numbers well above unity. This is indeed unfortunate since such formulas are intended to replace the creeping-flow forces in equations (6, 7) to enable point-particle simulations at particle Reynolds numbers of order 1. At even higher Reynolds numbers, fully resolved particle simulations might be the preferred choice, although such simulations also may face resolution challenges when an IB method is used to represent the surface of the individually moving particles.

References

[1] Andersson, H.I., Soldati, A.: Anisotropic particles in turbulence: status and outlook. *Acta Mech.* **224**, 2219-2223 (2013)

[2] Andersson, H.I., Jiang, F., Okulov, V.I.: Instabilities in the wake of an inclined prolate spheroid. In: Gelfgat, A. (ed.) *Computational Modelling of Bifurcations and Instabilities in Fluid Dynamics,* Computational Methods in Applied Sciences, Vol. 50, Chapter 9, pp. 311-352. Springer Nature (2019)

[3] Arcen, B., Ouchene, R., Khalij, M., Taniére, A.: Prolate spheroidal particles' behavior in a vertical wall-bounded turbulent flow. *Phys. Fluids* **29**, 093301 (2017)

[4] Ardekani, M.N., Costa, P., Breugem, W.P., Picano, F., Brandt, L.: Drag reduction in turbulent channel flow laden with finite-size oblate spheroids. *J. Fluid Mech.* **816**, 43-70 (2017)

[5] Balachandar, S.: A scaling analysis for point-particle approaches to turbulent multiphase flows. *Int. J. Multiphase Flow* **35**, 801-810 (2009)

[6] Balachandar, S., Eaton, J.K.: Turbulent dispersed multiphase flow. *Annu. Rev. Fluid Mech.* **43**, 111-133 (2010)

[7] Barboza, L.G., Gimenez, B.C.G.: Microplastics in the marine environment: current trends and future perspectives. *Marine Poll. Bull*. **97**, 5-12 (2015)

[8] Beckers, J. M.: Analytical linear numerical stability condition for an anisotropic three-dimensional advection-diffusion equation. *SIAM J. Numer. Anal.* **29**, 701-713 (1992)

[9] Brenner, H.: The Stokes resistance of an arbitrary particle IV: arbitrary fields of flow. *Chem. Eng. Sci.* **19**, 703-727 (1964)

[10] Challabotla, N.R., Zhao, L., Andersson, H.I.: Orientation and rotation of inertial disk particles in wall turbulence. *J. Fluid Mech.* **766**, R2 (2015)

[11] Do-Quang, M., Amberg, G., Brethouwer, G., Johansson, A.V.: Simulation of finite-size fibers in turbulent channel flows. *Phys. Rev. E* **89**, 013006 (2014)

[12] Durham, W.M., Climent, E., Barry, M., De Lillo, F., Boffetta, G., Cencini, M., Stocker, R.: Turbulence drives microscale patches of motile phytoplankton. *Nature Comm.* **4**, 2148 (2013)

[13] Eaton, J.K.: Two-way coupled turbulence simulations of gas-particle flows using point-particle tracking. *Int. J. Multiphase Flow* **35**, 792-800 (2009)

[14] El Khoury, G.K., Andersson, H.I., Pettersen, B.: Wakes behind a prolate spheroid in cross flow. *J. Fluid Mech.* **701**, 98–136 (2012)

[15] Eshghinejadfard, A., Hosseini, S.A., Thévenin, D.: Fully-resolved prolate spheroids in turbulent channel flows: a lattice Boltzmann study. *AIP Advances* **7**, 095007 (2017)

[16] Eshghinejadfard, A., Zhao, L., Thévenin, D.: Lattice-Boltzmann simulation of resolved oblate spheroids in wall turbulence. *J. Fluid Mech.* **849**, 510-540 (2018)

[17] Frölich, K., Schneiders, L., Meinke, M., Schröder, W.: Assessment of non-spherical point-particle models in LES using direct particle-fluid simulations. *AIAA Fluid Dynamics Conference*, Atlanta, Georgia, AIAA 2018-3714 (2018)

[18] Gallily, A.-H., Cohen, I.: On the orderly nature of the motion of nonspherical aerosol particles II Inertial collision between spherical large droplet and an axisymmetrical elongated particle. *J. Colloid Interface Science* **68**, 338-356 (1979)

[19] Happel, J., Brenner H.: Low Reynolds Number Hydrodynamics, 2nd Edition. Noordhoff International Publishing, Leyden (1973)

[20] Hölzer, A., Sommerfeld, M.: New simple correlation formula for the drag coefficient of non-spherical particles. *Powder Technol.* **184**, 361-365 (2008)

[21] Hölzer, A., Sommerfeld, M.: Lattice Boltzmann simulations to determine drag, lift and torque acting on non-spherical particles. *Comput. Fluids* **38**, 572–589 (2009)

[22] Jeffery, G. B.: The motion of ellipsoidal particles immersed in a viscous fluid. *Proc. R. Soc. Lond. A* **102**, 161-179 (1922)

[23] Jiang, F., Gallardo, J.P., Andersson H.I.: The laminar wake behind a 6:1 prolate spheroid at 45° incidence angle. *Phys. Fluids* **26**, 113602 (2014)

[24] Jiang, F., Gallardo J.P., Andersson H.I., Zhang, Z.: The transitional wake behind an inclined prolate spheroid. *Phys. Fluids* **27**, 093602 (2015)

[25] Jiménez, J.: Oceanic turbulence at millimeter scales. *Scientia Marina* **61**, 47-56 (1997)

[26] Lucci, F., Ferrante, A., Elghobashi, S.: Modulation of isotropic turbulence by particles of Taylor lenght-scale size. *J. Fluid Mech.* **650**, 5-55 (2010)

[27] Manhart, M., Tremblay, F., Friedrich, R.: MGLET: a parallel code for efficient DNS and LES of complex geometries. In: Parallel Computational Fluid Dynamics – Trends and Applications. Elsevier, Amsterdam, pp. 449-456 (2001)

[28] Marchioli, C., Fantoni, M., Soldati, A.: Orientation, distribution and deposition of elongated, inertial fibres in turbulent channel flow. *Phys. Fluids* **22**, 0333101 (2010)

[29] Maxey, M.: Simulation methods for particulate flows and concentrated suspensions. *Annu. Rev. Fluid Mech.* **49**, 171-193 (2017)

[30] Mortensen, P.H., Andersson H.I., Gillssen J.J.J., Boersma B.J.: Dynamics of prolate ellipsoidal particles in a turbulent channel flow. *Phys. Fluids* **20**, 093302 (2008)

[31] Ouchene, R., Khalij, M., Tanière, A., Arcen, B. : Drag, lift and torque coefficients for ellipsoidal particles: from low to moderate particle Reynolds numbers. *Comput. Fluids* **113**, 53-64 (2015)

[32] Ouchene, R., Khalij, M., Arcen, B., Tanière, A.: A new set of correlations of drag, lift and torque coefficients for non-spherical particles and large Reynolds numbers. *Powder Technol.* **303**, 33-43 (2016)

[33] Peller, N., Le Duc, A., Tremblay, F., Manhart, M.: High-order stable interpolations for immersed boundary methods. *Int. J. Numer. Meth. Fluids* **52**, 1175-1193 (2006)

[34] Richter, A., Nikrityuk, P.A.: Drag forces and heat transfer coefficients for spherical, cuboidal and ellipsoidal particles in cross flow at sub-critical Reynolds numbers. *Int. J. Heat Mass Transfer* **55**, 1343-1354 (2012)

[35] Sanjeevi, S.K.P., Padding, J.T.: On the orientational dependence of drag experienced by spheroids. *J. Fluid Mech.* **820**, R1 (2017)

[36] Sanjeevi, S.K.P., Kuipers, J.A.M., Padding, J.T.: Drag, lift and torque correlations for non-spherical particles from Stokes limit to high Reynolds numbers. *Int. J. Multiphase Flow* **106**, 325-337 (2018)

[37] Schiller, L., Naumann, A.Z.: Über die grundlegenden Berechnungen bei der Schwerkraftaufbereitung. Z. *Ver. Deutsch Ing.* **77**, 318-320 (1933)

[38] Schneiders, L., Meinke, M., Schröder, W.: Direct particle-fluid simulation of Kolmogorov-length-scale size particles in decaying isotropic turbulence. *J. Fluid Mech.* **819**, 188-227 (2017a)

[39] Schneiders, L., Meinke, M., Schröder, W.: On the accuracy of Lagrangian point-mass models for heavy non-spherical particles in isotropic turbulence. *Fuel* **201**, 2-14 (2017b)

[40] Shaw, R.A.: Particle-turbulence interactions in atmospheric clouds. *Annu. Rev. Fluid Mech.* **35**, 183-227 (2003)

[41] Siewert, C., Kunnen, R.P.J., Meinke, M., Schröder, W.: Orientation statistics and settling velocity of ellipsoids in decaying turbulence. *Atmos. Res.* **142**, 42-56 (2014)

[42] Sommerfeld, M., van Wachem, B., Oliemans, R.: Best practice guidelines for computational fluid dynamics of dispersed multiphase flows. ERCOFTAC (2008)

[43] Sommerfeld, M., Qadir, Z.: Fluid dynamic forces acting on irregular shaped particles: simulations by Lattice-Boltzmann method. *Int. J. Multiphase Flow* **101**, 212-222 (2018)

[44] Tavakol, M.M., Abouali, O., Yaghoubi, M., Ahmadi, G.: Dispersion and deposition of ellipsoidal particles in a fully developed laminar pipe flow using non-creeping formulations for hydrodynamic forces and torques. *Int. J. Multiphase Flow* **75**, 54-67 (2015)

[45] van Dyke, M.: An Album of Fluid Motion. The Parabolic Press, Stanford, California (1982)

[46] van Wachem, B., Zastawny, M., Zhao, F., Mallouppas, G.: Modelling of gas-solid turbulent channel flow with non-spherical particles with large Stokes numbers. *Int. J. Multiphase Flow* **68**, 80-92 (2015)

[47] Voth, G.A., Soldati, A.: Anisotropic particles in turbulence. *Annu. Rev. Fluid Mech.* **49**, 249-276 (2017)

[48] Williamson, J.H.: Low-storage Runge-Kutta schemes. *J. Comput. Phys.* **56**, 48-56 (1980)

[49] Xia, J., Luo, K., Fan, J.: A ghost-cell based high-order immersed boundary method for inter-phase heat transfer simulation. *Int. J. Heat Mass Transfer* **75**, 302-312 (2014)

[50] Zastawny, M., Mallouppas, G., Zhao, F., van Wachem, B.: Derivation of drag and lift force and torque coefficients for non-spherical particles in flows. *Int. J. Multiphase Flow* **39**, 227–239 (2012)

[51] Zhang, H., Ahmadi, G., Fan, F.-G., McLaughlin J.B.: Ellipsoidal particles transport and deposition in turbulent channel flows. *Int. J. Multiphase Flow* **27**, 971-1009 (2001)